Multifunctional cellular sandwich structures with optimised core topologies for improved mechanical properties and energy harvesting performance

Boyue Chen [a], Yu Jia[b*], Fumio Narita[c], Congsi Wang[d], Yu Shi[a**]

[a]*Department of Mechanical Engineering, University of Chester, Pool Lane, Chester, UK*

[b]*School of Engineering and Applied Science, Aston University, Birmingham, UK*

[c]*Department of Frontier Sciences for Advanced Environment, Graduate School of Environmental Studies, Tohoku University, Aoba-yama-6-6-02, Sendai, Japan*

[d]*School of Electromechanical Engineering, Xidian University, Xi'an, No.2 Taibai South Road 710071, China*

Abstract

This paper developed a multifunctional composite sandwich structure with optimised design on topological cores. As the main concern, full composite sandwich structures were manufactured with carbon fibre reinforced polymer (CFRP) facesheets and designed cores. Three-point bending tests have been performed to assess the mechanical performance of designed cellular sandwich structures. To evaluate the energy harvesting performance, the piezoelectric transducer was integrated at the interface between the upper facesheet and core, with both sinusoidal base excitation input and acceleration measured from real cruising aircraft and vehicle. It has been found that the sandwich with conventional honeycomb core has demonstrated the best mechanical performance, assessed under the bending tests. In terms of energy harvesting performance, sandwich with re-entrant honeycomb manifested approximately 20% higher RMS voltage output than sandwiches with conventional honeycomb and chiral structure core, evaluated both numerically and experimentally. The resistance sweep tests further suggested that the power output from sandwich with re-entrant honeycomb core was twice as large as that from sandwiches with conventional honeycomb and chiral structure cores, under optimal external resistance and sinusoidal base excitation.

*Corresponding author. School of Engineering and Applied Science, Aston University, Birmingham,Uk

**Corresponding author. Department of Mechanical Engineering, University of Chester, Chester, Uk

Email address: y.jia1@aston.ac.uk (Y. Jia), y.shi@chester.ac.uk (Y. Shi)

Keywords: A. Polymer-matrix composites (PMCs), A. Smart materials, B. Vibration, Piezoelectric energy harvesting

1. Introduction

Advanced composite materials, such as carbon fibre reinforced polymers (CFRPs), have been widely employed in aerospace, automotive and offshore wind energy sectors due to their high strength-to-weight ratio with better damping behaviour than conventional metallic material [1–4]. In addition to the benefits of lightweight and improved mechanical behaviour, the multifunctional composite with one or several non-structural functionalities have been developed. For instance, the composite is integrated with nano-electronics and/or transducers, energy storage and energy harvesters [5–8]. In particular, the combination of energy harvesting with mechanically improved composite structure would scavenge the energy from the wasted kinematic motion (e.g. vibration), which could potentially help to achieve the self-powered sensing applied in a relatively harsh environment [9, 10].

Vibration might be the most abundant, which is barely avoided during service. Vibrational energy could be harvested through the electromagnetic [11,12] or piezoelectric principle [13-15]. Therefore, the multifunctional composite with energy harvesting capability could be fabricated by the different schemes. The piezoelectric elements, such as ZnO nanowires, have been reported to be hydrothermally grown onto the aramid fabrics as a composite energy generator[16]. Alternatively, a sandwich structure was developed by embedding the piezoelectric component between two composite laminates [16–18]. The direct integration of macro fibre composite (MFC) with the composite laminate for harvesting energy was also experimentally [20] and numerically [21] assessed based on the various vibration inputs at different application scenarios.

For engineering composite, the cellular sandwich structures could have been most popular due to their lightweight and impressive mechanical performance. Honeycomb, inspired from the natural design, might be the most common core applied as primary structure with the excellent energy absorption, vibration damping, electromagnetic interference (EMI) and acoustic absorption. Auxetic structure was recently

developed as engineering material due to their characteristics of the negative Poisson's ratio. Auxetic material has received interests in multiple applications, such as medical, energy absorbers, sports and military [21, 22]. However, the use of auxetic feature in piezoelectric energy harvesting was rarely reported [24]. Taking advantage of the mechanical feature of the auxetic structure, the in-plane strains could be superimposed, instead of compensating each other when non-auxetic material is used. Based on this principle, a numerical work utilising PVDF transducer with an elliptical-voided beam was developed where 17.4 μW achieved, demonstrating a 1.59 times enhancement than that of using non-voided substrate [24]. The further investigation on boosting the energy harvesting from different auxetic designs was progressed [24–26]. A circular auxetic topology was numerically studied most recently in combination of multi-types of transducers and substrate materials [28].

Although the energy harvesting potential was proven, the proposed structures previously have not well considered the improvement of mechanical property together since it is important to be applied as the primary load-carrying structure. Therefore, in this paper, a variety of auxetic and non-auxetic cellular structures were designed and numerically and experimentally assessed for both static mechanical performance and dynamic energy harvesting behaviour. The piezoelectric transducer, macro fibre composite (MFC), was used to be integrated between the upper facesheet and the core, for experimentally measuring the energy outputs harvested from the predefined vibration inputs. This work eventually would target at development of a multifunctional cellular sandwich structure with optimised facesheet and designed core to maximise the mechanical performance and energy harvesting behaviour for self-powering wireless sensor nodes used in future transportation or energy application.

2. Materials design and experiments

2.1 Topological design of cellular cores

In this work, three types of topological cores were designed as the conventional honeycomb, re-entrant honeycomb and chiral structure, as shown by Fig. 1.

The dimensions of individual cellular core for mechanical and energy harvesting tests are listed in Table 1, which refers to the standards of ASTM C393 [29] for three-point bending testing. The wall thickness varied

among different topologies to ensure the same relative density, so that direct comparison was legitimate, as is shown in Table 1. The relative density in Table 2 was defined as:

$$\rho_{rel} = \frac{\rho}{\rho_s} \tag{1}$$

Where ρ is the density of the cellular structure and ρ_s is the density of the constituent material, in this paper Acrytlonitrile butadiene styrene (ABS) [30].

The in-plane mechanical properties of the core topologies, such as the in-plane Poisson's ratio and the Young's modulus towards the sandwich longitudinal direction (direction 1 in Figure 1), played important roles in the mechanical and power generation performance of the sandwiches. Therefore, the in-plane Poisson's ratio and the Young's modulus in direction 1 were calculated via Eq.2-5 and recorded in Table 2.

The effective Young's modulus and Poisson's ratio of honeycomb structures have been well investigated in Gibson's theory [31]:

$$E_1^{eff} = \left(\frac{t}{l}\right)^3 \frac{\left(\frac{h}{l} + \sin(\theta)\right)}{cos^3(\theta)} E_s \tag{2}$$

$$v_{12}^{eff} = \frac{cos^2(\theta)}{\left(\frac{h}{l} + \sin(\theta)\right)\sin(\theta)} \tag{3}$$

The geometric parameters t, l, h and θ were denoted in Figure 1 (a), (b) and (c). E_s was the Young's modulus of the constituent material [30].

In order to predict the E_1^{eff} and v_{12}^{eff} of the chiral structure, a simplified finite element (FE) model constituting a chiral unit cell was built, with boundary conditions and loadings illustrated in Figure 1 (d). The E_1^{eff} and v_{12}^{eff} of the chiral structures were defined following [32]:

$$E_1^{eff} = \frac{\frac{F}{hW}}{\frac{\Delta U}{U}} \tag{4}$$

$$v_{12}^{eff} = -\frac{\frac{\Delta W_1 - \Delta W_2}{W}}{\frac{\Delta U}{U}} \tag{5}$$

Where F was the loading on the chiral unit cell in direction 1. U, W, ΔU, ΔW_1 and ΔW_2 were the overall dimensions of the unit cell and the deformation, defined in Figure 1 (d). h is the thickness of the chiral core.

Unidirectional carbon fibre reinforced polymer (CFRP) with layup designs of $[0/90]_s$ and $[45/-45]_s$ were designed and manufactured as facesheet of the cellular sandwich structures. Composites with $[0/90]_s$ would have fibres oriented in sandwich longitudinal directions, leading to high flexural stiffness. Therefore, composite panels with $[0/90]_s$ layup was selected to sandwich the designed topological cores to characterise their mechanical performance under three-point bending. Oppositely, composite panels with $[45/-45]_s$ layups had a lower flexural stiffness, which potentially leads to a higher deformation and power output in energy harvesting test. So in the energy harvesting experiment, composite panels with $[45/-45]_s$ layup were used as facesheets. The individual CFRP facesheet was trimmed to be 230 mm x 47 mm with 1mm in thickness to match the cores for testing, following the dimension design protocols stated in standard ASTM C393 [29].

2.2 Fabrication of multifunctional cellular sandwich structures

As introduced in 2.1, the unidirectional carbon fibre epoxy prepreg (Easycomposite, UK) was manufactured for laminate facesheet in a programmable oven with the designed layups. The topological cores were 3D printed by Pro2 Plus (Raise3d) with thermoplastic polymer, Acrylonitrile Butadiene Styrene (ABS), selected due to its relatively high mechanical performance and glass transition temperature (105 ° C) to be compatible with curing cycle for integration of facesheets by adhesive film, XA120.

The cellular sandwich composite structure was cured by heaten press at 85 °C with pressure of 0.75 bars for 6 hours [33].

To assess their performance on energy harvesting, the macro fibre composite (MFC) P2-8528 was applied at the interface between upper facesheet and core (See Fig. 2), as the piezoelectric energy harvester in vibration testing. Metallic wires were connected to the electrodes of the MFC by silver paste. In order to avoid any residual stress potentially produced at the interface between the facesheet and core, a thin slot with 110mm long and 0.3mm in thickness was pre-designed on the top surface of the core during 3D

printing, aiming at perfectly fit to the size of MFC. It is also worthy to note that a thin Kapton film layer (25 μm thick) was placed between MFC and upper CFRP facesheet to avoid short circuit due to contact between wires and carbon fibres (see Fig. 2).

2.3 Experimental setup and characterisation

2.3.1 Three-point bending tests

The three-point bending tests were conducted by Instron 3367 with a load-cell of 30 kN based on ASTM C393 [29]. The supporting span in three-point bending test was adjusted with a distance of 150 mm while a loading rate of 2 mm/min was applied. For testing the individual cellular topology and sandwich structure design, each experiment was repeated at least three times to ensure the experimental reliability.

To quantify the crashworthiness of the structure, crushing force efficiency (CFE) is used in this work with definition by Eq. 6:

$$CFE = \frac{F_{ave}}{F_{max}} = \frac{\frac{1}{d}\int_0^d F(x)dx}{F_{max}} \tag{6}$$

Where F_{ave} is the average force until final collapse of the structure while F_{max} is the maximum loading. d is the displacement when it has finally collapsed.

Energy absorption (EA) is obtained by integrating load variables over the displacement evolved during the whole testing process; the specific energy absorption (SEA) is an energy absorption to weight ratio which represents the absorbed energy per mass of the structure:

$$EA = \int_0^d F(x)dx \tag{7}$$

$$SEA = \frac{\int_0^d F(x)dx}{m} \tag{8}$$

m in Eq. 8 refers to the mass of cellular or sandwich structures under investigation. All the parameters mentioned above were evaluated for all mechanical tests and discussion was made in the following sections.

2.3.2 Energy harvesting

To experimentally assess the energy harvesting behaviour, the multifunctional sandwich structure was clamped by polylactide (PLA) fixture, which was manufactured by 3D printing. The clamping distance was 35 mm, in order to ensure stable clamping and have MFC closer to the clamping end. In this regard, larger stress would present in MFC during vibration, which enhanced voltage output. The clamper was anchored in an electrodynamic shaker (LDS 406, Brüel & Kjaer). A functional generator (33210 A, Agilent Technologies) via a power amplifier (LDS PA100E, Brüel & Kjaer) was connected to shaker to properly control the vibration input of testing. A variable resistance box was connected in parallel to the MFC transducer to apply resistance sweep and voltage measurement was recorded by a digital oscilloscope (DSO-X-2004A, Agilent Technologies). A commercial accelerometer (ADXL 325) was mounted on the clamper to monitor the input excitation, whose signal was recorded by another channel in the same digital oscilloscope. The test rig is schematically illustrated by Fig. 3. Sinusoidal excitation with a variety of frequencies was applied to the clamping end of the samples in sequence to determine the 1^{st} bending mode resonant frequency, under 10 MΩ, which was close to open-circuit condition. For clamped-free cantilever beam structure, typically only the first bending mode is ideal for vibrational energy harvesting because in the higher modes partial charge cancellation would occur due to the opposite stress existing in a single piezoelectric transducer [21]. After determining the open-circuit resonant frequency, resistance sweep was conducted on samples with different core topologies to determine the maximum generated power and the optimum external resistance. In cases of all samples, sinusoidal excitation of three amplitudes, namely 1 g, 1.5 g and 2 g (Peak-to-peak) were applied and result investigated. Under resonant frequency, the optimum external electrical resistance was found by a resistance sweep via the variable resistance box, and the maximum output power was obtained. 1 g, 1.5 g and 2 g (Peak-to-Peak) sinusoidal excitations were applied to all samples, which were typical in piezoelectric transducers assessment [34,35]. The voltage response to the sinusoidal vibrations were validated by the numerical calculation. Afterwards, the energy harvesting potential of sandwiches with different core topologies was tested under vibration of industrial environment, which was measured in an aircraft and a vehicle, respectively.

3 Computational modelling

3.1 FE model for prediction of three-point bending

FE analysis was utilised to study the stress distribution in sandwich structures under three-point bending. The model was built in COMSOL Multiphysics 5.5, with solid mechanics physics involved.

In the case of three-point bending test, the sandwich structures were mounted on two fixed rigid supporting rollers with a span of 150 mm, same as the experimental setup. Another rigid loading roller was responsible for imposing vertical displacement on the sandwich structure. The boundary conditions (BCs) for three-point bending models are schematically illustrated in Fig. 4 (a).

The mechanical properties of CFRP laminas and ABS cellular structures are presented in Table 2, which were suggested by the suppliers [30,36].

3.2 FE model for prediction of energy harvesting

The mechanical, piezoelectric and dielectric properties of MFC P2-8528 are listed in Table 2 [37]. To simulate the real test condition, clampers were also included and anchored via a pinhole. MFC was modelled as a piezoelectric patch of its effective area (85×28 mm^2) and 0.3 mm thickness [21]. The external excitation was defined as a body load whose amplitude was consistent with the experimental level [38].

Within COMSOL Multiphysics 5.5, Piezoelectric device Multiphysics was implemented. This module constitutes a combination of solid mechanics physics to model the mechanical behaviour and electrostatics physics to monitor the electrical response of MFC. One side of the MFC was set to be 'Ground' and the other to be 'Floating potential' so that the open-circuit voltage output could be obtained.

'Eigenfrequency' study was employed to obtain the natural frequencies of different modes and the mode shapes. The solution of the 'eigenfrequency' study was fed into 'frequency domain modal' study to investigate the steady-state open-circuit voltage response. Damping ratio of 1^{st} resonant bending mode was measured from experiment and used in the modal solver. To study the contribution of stress distribution in auxetic structure to power output enhancement, the stress towards the two in-plane directions was numerically calculated. A static body load was applied to the structure, so that any dynamic factors, such as damping loss, would not be involved to interfere the analysis. The model geometry and

anchor position were same as the model for eigenfrequency simulation. The stress distribution in the two in-plane directions were recorded and compared between sandwiches with different core topologies.

4. Result and discussion

4.1 Three-point bending mechanical investigation on composite sandwich structure: core topologies investigation

Composite panels with $[0/90]_s$ layup would have carbon fibres oriented parallel to the longitudinal direction, contributing to a large flexural stiffness. Therefore, $[0/90]_s$ facesheets were selected to sandwich conventional honeycomb, re-entrant honeycomb and chiral structure to evaluate the effect of core topologies on three-point bending response. The load-displacement curves are illustrated in Fig. 5.

Sandwiches with all three types of core topologies exhibited similar failure mechanisms. In Fig. 5, stage A corresponded to the elastic bending stage under three-point bending, and stage B denoted all the bending response after the end of elastic bending stage, including debonding initiation and propagation. Interestingly, the curves belonging to sandwiches with re-entrant honeycomb and chiral structure cores indicated further increase after the end of the elastic bending stage, until the debonding initiation at the maximum loading (shown in the experimental observation at the top of Fig. 5). This observation was probably resulted from the micro-cracks developed as the loading increased. The accumulation of these micro-cracks finally led to the occurrence of the debonding. The experimental observation at the top of Fig. 5 demonstrated that, for sandwiches with cores by all topologies, the debonding occurred in region between the loading and supporting roller. This was consistent with the finite element out-of-plane shear stress prediction in Fig. 6 (b), (c) and (d), which indicated that the stress-rich region matched the location where debonding started.

The debonding continued to extend until finally reaching the tip of the sandwich structures, denoted by experimental observation in the right parts of Fig. 5. The debonding propagation process was in company with stage B of all curves in Fig. 5. Upon final failure, no core shear fracture was observed. In addition, it was found that during debonding propagation, sandwich with chiral structure exhibited lower load-bearing capacity compared to sandwiches with cores by other two topologies. Chiral structure, due to its

topological nature, had worse unit cell connectivity compared to the honeycomb structures (both conventional and re-entrant honeycombs). To be specific, the only connections between neighbouring unit cells, in the case of chiral structure, are the corner points, while for honeycomb structures, all wall ligaments are shared by neighbouring unit cells. Therefore, shear stress transfer would be less efficient for sandwich for chiral structure core, leading to its inferior load bearing capacity during debonding propagation.

Table 3 lists the rigidity, maximum loading, crashing force efficiency (CFE), energy absorption (EA) and specific energy absorption (SEA) of sandwiches with conventional honeycomb, re-entrant honeycomb and chiral structure under three-point bending tests, respectively. It was demonstrated in Table 3 that sandwiches with conventional and re-entrant honeycombs exhibited the highest and lowest rigidity and maximum loading, respectively. The rigidity ranking among the sandwiches with the three kinds of topologies was consistent with the unit cell stiffness prediction, listed in Table 2. It should be noted that it is the facesheet that mainly contributes to the flexural stiffness of the sandwich structures. Since cores of all topologies investigated in this study were sandwiched by CFRP facesheets of the same layup, the rigidity discrepancy between sandwiches with different core topologies were much less significant than their difference in the unit cell stiffness.

The stress distribution predicted by FE simulation in Fig. 6 (a) indicated that the sandwich with conventional honeycomb core sustained a lower out-of-plane shear stress at the interface between the core and the facesheet. Since Mode II shear debonding is mainly triggered by excessive out-of-plane shear stress at the interface, it could be deduced from the FEA stress prediction that sandwich with conventional honeycomb core was least susceptible to Mode II shear debonding failure. This might explain its high maximum loading before debonding initiation.

Moreover, the sandwich with conventional honeycomb also demonstrated the highest energy absorption (EA) and specific energy absorption (SEA), proving its superior energy absorption capacity compared to sandwiches with cores by other two topologies (Table 3). The load-displacement curves Fig. 5 showed that sandwich with conventional honeycomb absorbed more energy in the elastic bending stage than sandwiches with cores by other two topologies, thanks to its high rigidity and maximum loading. After

failure initiation, however, the load bearing capacity between sandwiches with conventional and re-entrant honeycombs in the plateau stage B was almost the same, and slightly higher than sandwich with chiral structure core. This observation indicated that the superiority of energy absorption of sandwich with conventional honeycomb core mainly stemmed from its excellent mechanical performance in the elastic bending stage. In the meantime, this observation also explained the lower crashing force efficiency (CFE) of sandwich with conventional honeycomb core compared to other two topologies, as CFE was defined as the ratio between the average loading across the whole displacement span and the maximum loading.

Aside from the superiority of energy absorption performance from the sandwich with conventional honeycomb core, it is also interesting to notice that sandwiches with chiral structures and re-entrant honeycomb cores demonstrated similar energy absorption capacity (Table 3). According to Table 3, sandwich with chiral structure outstood the re-entrant honeycomb core in the maximum loading (stage A in Fig. 5), but its load bearing capacity degraded more significantly after reaching the plateau stage (stage B). In other words, the mechanical advantage of sandwich with chiral structure core from the elastic bending stage A was offset by its inferior mechanical performance in stage B, compared to sandwich with re-entrant honeycomb core. As discussed above, the excessive degradation of load-bearing capacity in the case of chiral structure could be explained by the poor interconnection between neighbouring unit cells.

4.2 Energy harvesting investigation on composite sandwich with different core topologies

4.2.1 Sinusoidal excitation

$[45/-45]_s$ facesheet exhibited lowest bending stiffness, which made it most suitable as substrate for vibrational energy harvesting. Therefore, sandwiches with $[45/-45]_s$ and different core topologies were selected for energy harvesting characterisation. Figure 7 illustrates the first resonant mode shapes of sandwiches with conventional honeycomb core, re-entrant honeycomb core and chiral structure core, respectively. For clamped-free cantilever beam structure, typically only the first bending mode is ideal for vibrational energy harvesting because in the higher modes partial charge cancellation would occur due to

the stress of opposite signs existing in a single piezoelectric transducer [21]. The numerical prediction, together with the experimental observation of the 1st bending mode resonant frequency are listed in Table 4. The measured 1st bending resonant frequencies for sandwiches with conventional honeycomb, re-entrant honeycomb and chiral structures were 32, 37, 32 Hz, respectively, while the finite element prediction gave 41, 40, 40 Hz. It was found that the simulation inclined to give larger the 1st bending mode natural frequencies than the experiments. The deviation could also result from difference in clamping, fabrication tolerance, material properties and measurement uncertainty. For example, unexpected core-facesheet junctions occurred during heat pressing process at the location of MFC slots, which is not involved in the FE model (Fig. 8).

The measured damping ratios are listed in Table 4. The re-entrant honeycomb sandwich exhibited lower 1st mode damping (0.041) than both conventional honeycomb sandwich (0.046) and chiral structure sandwich (0.048). This comparison indicated that sandwich with conventional honeycomb and chiral structure cores were able to provide with more damping around the 1st bending mode resonance, so that vibrational amplitude can be better controlled to avoid structural failure [39]. But in contrast, it also implied that more mechanical energy might be wasted instead of being transduced into the electrical domain to be scavenged, and the attenuation effect of damping is far more significant at on-resonance than off-resonance.

The measurement and numerical calculation of the open-circuit RMS voltage for sandwiches with different core topologies are plotted in Fig. 9, with results at resonance summarised in Table 4. The measured voltage was derived when the base excitation was 1 g peak-to-peak sinusoidal waves and the external resistance was 10 MΩ, which was close to the open-circuit condition compared to the impedance of the MFC transducers (approximately 20 kΩ, which will be discussed later). It was found from Fig. 9 and Table 4 that the mismatch of open-circuit RMS voltage outcome between measurement and simulation was below 10%. Therefore, it was concluded that the measurement results were well validated, so that further experimental investigation could be carried on.

To compare the power generation performance between sandwiches with different core topologies, resistance sweeps were conducted experimentally, and the power generated is plotted in Fig. 10. The

measured optimum resistance was 20 kΩ in all three cases. The theoretical optimum resistance, at which the external load should match the MFC impedance, was calculated as $Z_{mat}=1/(2\pi f*C)$, where f is the excitation frequency and C is the capacitance of the MFC transducers. The calculated values for sandwiches with conventional honeycomb and chiral structure cores were both 26.7 kΩ, and sandwich with re-entrant honeycomb was 23.2 kΩ, which proved that the measurement of 20 kΩ as optimum external resistance was legitimate.

The generated power was calculated by $P = V_{Rms}^2/R$. It can be observed from Fig. 10 that sandwich with re-entrant honeycomb could generate 24.4 μW under optimum resistance (20 kΩ), higher than the case of chiral structure (12.0 μW, under 20 kΩ) and conventional honeycomb (14.4 μW, under 20 kΩ). All power output was derived under 1 g peak-to-peak sinusoidal excitation of resonant frequencies of each sandwich structure. The superiority of sandwich with re-entrant honeycomb core in terms of energy harvesting was, first of all, associated with the low damping ratio, as was listed in Table 4. Besides, in order to ensure approximately identical relative density, re-entrant honeycombs should have relatively lower wall thickness due to its dense unit cell arrangement. This led to a low flexural stiffness, as listed in Table 2 which was favourable in power generation. Thirdly, according to Table 2, re-entrant honeycomb exhibited a strong auxetic behaviour (in-plane Poisson's ratio -1.29) compared to the non-auxetic conventional honeycomb (0.69) and only weakly auxetic chiral structure (-0.07). The auxetic structures stretched/compressed the MFC transducer in the transverse direction when the MFC transducer was at the tension/compression sides under bending. Since the d_{32} and d_{31} piezoelectric coefficient were of same sign, the auxetic behaviour alleviated the offsetting influence from d_{32}, or even enhance the overall voltage output.

It has been reported that the main advantage of implementing auxetic structures is that the piezoelectric transducer is under stress of same sign in both in-plane directions that are orthotropic to each other, as can be emphasised mathematically [23, 27]:

$$P_{max} \propto (\sigma_{11} + \sigma_{22})^2 \tag{9}$$

In which σ_{11} and σ_{22} are the stress towards the two in-plane directions respectively. To study the stress distribution within the MFC transducer, a simplified FE simulation, with only static loading applied to the sandwich structures, was performed. Volume average stress within the transducer was calculated and listed in Table 5. It can be observed that the coupled average stress in the case of re-entrant honeycomb sandwich was slightly higher than the case of chiral structure and conventional honeycomb. This indicated that the auxetic core design contributed to the superiority of re-entrant honeycomb sandwich in energy harvesting. However, in all the three cases, σ_{11} and σ_{22} had opposite signs, regardless auxetic or not. The first reason for this might be the non-auxetic feature of facesheet, which constraint the extension (contraction) towards the transverse direction when the MFC transducer is at tension (compression) side during bending. In addition, it has been revealed that the transducer needs to be compliant enough compared to the substrate to be compatible with the deformation of auxetic substrate [24]. Although the flexibility of MFC has been widely acknowledged (30.34 GPa longitudinal Young's modulus [21]), the compliance of MFC might still be not enough to let it deform compatibly with the auxetic core, compared to PVDF which has been used in [24] and [26] (2.74 GPa Young's modulus).

Figure 11 proves that the output power can be remarkably magnified with increase of input acceleration. At 2 g peak-peak input acceleration, the maximum was as large as 85 μW for sandwich with re-entrant honeycomb, 37 μW for chiral structure and 46 μW for conventional honeycomb. All the output demonstrated were obtained when the sandwich structures were excited under resonant frequencies. The power output was achieved at 20 kΩ optimum external resistance.

The results from some of existing works investigating the effect of substrate auxetic design on the enhancement of piezoelectric energy harvesting are listed in Table 6. Compared to the existing outcome, the output from the present work was comparable to those whose excitation scheme was resonant vibration but lower than the rest. It should be noticed that the final output was dependent on a variety of factors from material of substrate and transducer to the choice of excitation scheme. In addition, it is interesting to observe that the boosting factor in the existing works could be as large as 10 or 12 times compared to their non-auxetic counterpart [24, 27]. And in the present work, the sandwich with re-entrant honeycomb exhibited 2 times larger power output compared to sandwich with the non-auxetic

conventional honeycomb. It should be noted that in all works listed in Table 6, power output from auxetic design was compared to void-free substrates. This suggests that not only auxetic feature but also stress concentration due to the existence of corners and thin ribs in the substrates contributed to the output enhancement. The later factor, however, was not involved in the present work.

4.2.2 Vibration data

To assess the energy harvesting potential of sandwiches in real industrial environment, acceleration measured from a CGJ type aircraft and a BWM vehicle were loaded to the electrodynamic shaker. The Short-time Fourier Transform (STFT) of the acceleration signals was recorded in Fig. 12 to explain the evolution of frequency spectrum with time. The aerospace data was collected when the aircraft was in-flight, and was broadband and noisy from 0 to 2 kHz (Fig. 12 (a)) [20, 21]. The mean acceleration level was around 14 g. Figure 12 (b) was the x-axis acceleration running along the BWM vehicle, when measurement unit was located under the bonnet near the engine. The signal demonstrated a first harmonic peak at around 33 Hz in the whole time span of measurement. This corresponded to the engine rotation speed. In addition to this, higher order harmonic peaks were also observed, occurring with a certain time interval. The mean acceleration level was 1.19 g. Acceleration signals from Y-axis (running across the vehicle) and Z-axis (upright direction) were relatively broadband, both with mean acceleration level around 1.57 g [19, 20].

The acceleration level mentioned above exceeded the capacity of the electrodynamic shaker. Therefore, several measurement points were taken within the capacity and power fit was performed to predict the power generated at full acceleration amplitude. The estimated power output is listed in Table 7. When excited by aerospace-level vibration, sandwich with re-entrant honeycomb produced as high as 33.26 mW power, more than 50% larger than the power generated by the sandwiches with non-auxetic honeycomb core chiral structure. Similarly, sandwich with re-entrant honeycomb core outstood sandwiches with other topologies under acceleration collected in the BWM vehicle. Estimation of 344.39 μW, and 204.91 μW power were obtained under acceleration towards x and z-axis, respectively, which were both larger than its non-auxetic counterpart and chiral structures. Under acceleration excited

towards y-axis, sandwich with conventional honeycomb exhibited slightly higher predicted power generation than that with re-entrant honeycomb, which was likely the consequence of power fit.

5. Conclusion

This paper uniquely presented extensive studies on the mechanical properties and energy harvesting potential of different cellular topologies and sandwich structures. First of all, sandwiches with conventional honeycomb, re-entrant honeycomb and chiral structure cores and CFRP facesheets with $[0/90]_s$ layup were evaluated in terms of three-point bending response. The mechanical assessment mentioned above was assisted by FE simulation of stress distribution to understand the initiation of failure. The failure mechanism and comparison between core topologies were discussed thoroughly. With respect to energy harvesting characterisation, experimental and numerical studies were conducted based on sandwiches with different core topologies and $[45/-45]_s$ facesheets, integrated with MFC transducers.

It has been found that sandwich with conventional honeycomb exhibited superiority in mechanical performance under three-point bending, over sandwiches with other core topologies. Specifically, the sandwich with conventional honeycomb core was able to absorb 1.88 J energy upon final failure, higher than sandwich with re-entrant honeycomb core (1.66 J) and chiral structure (1.69 J). Its superiority mainly stemmed from its better stiffness and higher maximum loading. Under resonant frequency (37 Hz) and optimum resistance (20 kΩ), sandwich with re-entrant honeycomb and $[45/-45]_s$ facesheets could harvest 24.4 μW power under 1 g peak-to-peak sinusoidal acceleration, better than the cases of conventional honeycomb (14.4 μW) and chiral structure (12.0 μW). Under real industrial environment, sandwich with re-entrant honeycomb core and $[45/-45]_s$ facesheets also demonstrated best energy scavenging performance. Power output of 33.26 mW could be obtained under acceleration (mean acceleration level of 14.02 g) measured in the aircraft, and highest output of 692.22 μW was estimated under automotive-level vibration (acceleration towards y-axis, with mean level of 1.57 g). The proposed concept in this paper can be utilised in application such as aerospace and automatic where self-powering and mechanical property are both required.

Acknowledgements

This research did not receive any specific grant from funding agencies in the public, commercial, or not-for-profit sectors.

References

[1] Yang M, Hu Y, Zhang J, Ding G, Song C. Analytical model for flexural damping responses of CFRP cantilever beams in the low-frequency vibration. J Low Freq Noise Vib Act Control 2018;37:669–81. https://doi.org/10.1177/1461348418756024.

[2] Shi Y, Swait T, Soutis C. Modelling damage evolution in composite laminates subjected to low velocity impact. Compos Struct 2012;94:2902–13. https://doi.org/10.1016/j.compstruct.2012.03.039.

[3] Srivastava VK, Gries T, Veit D, Quadflieg T, Mohr B, Kolloch M. Effect of nanomaterial on mode I and mode II interlaminar fracture toughness of woven carbon fabric reinforced polymer composites. Eng Fract Mech 2017;180:73–86. https://doi.org/10.1016/j.engfracmech.2017.05.030.

[4] Hwang JH, Jin CK, Seo HY, Kang CG. Effect of the number of CFRP prepregs and roughness at the bonding area on the spring-back and flexural strength of hybrid composites of CFRP combined with CR980. Metals (Basel) 2019;9. https://doi.org/10.3390/met9101054.

[5] Gibson RF. A review of recent research on mechanics of multifunctional composite materials and structures. Compos Struct 2010;92:2793–810. https://doi.org/10.1016/j.compstruct.2010.05.003.

[6] Muralidharan N, Teblum E, Westover AS, Schauben D, Itzhak A, Muallem M, et al. Carbon Nanotube Reinforced Structural Composite Supercapacitor. Sci Rep 2018;8:1–9. https://doi.org/10.1038/s41598-018-34963-x.

[7] Yu Y, Zhang B, Feng M, Qi G, Tian F, Feng Q, et al. Multifunctional structural lithium ion batteries based on carbon fiber reinforced plastic composites. Compos Sci Technol 2017;147:62–70. https://doi.org/10.1016/j.compscitech.2017.04.031.

[8] González C, Vilatela JJ, Molina-Aldareguía JM, Lopes CS, LLorca J. Structural composites for multifunctional applications: Current challenges and future trends. Prog Mater Sci 2017;89:194–251. https://doi.org/10.1016/j.pmatsci.2017.04.005.

[9] Farrar CR, Park G, Rosing T, Todd MD, Hodgkiss W. Energy harvesting for structural health monitoring sensor networks. Struct Heal Monit 2007 Quantif Validation, Implement - Proc 6th Int Work Struct Heal Monit IWSHM 2007 2007;2:1773–80. https://doi.org/10.1061/(asce)1076-0342(2008)14:1(64).

[10] Ball AD, Gu F, Cattley R, Wang X, Tang X. Energy harvesting technologies for achieving self-powered wireless sensor networks in machine condition monitoring: A review. Sensors (Switzerland) 2018;18. https://doi.org/10.3390/s18124113.

[11] Yang B. Hybrid energy harvester based on piezoelectric and electromagnetic mechanisms. J Micro/Nanolithography, MEMS, MOEMS 2010;9:023002. https://doi.org/10.1117/1.3373516.

[12] Rajarathinam M, Ali SF. Investigation of a hybrid piezo-electromagnetic energy harvester Untersuchung eines hybriden piezo-elektromagnetischen Energy-Harvesters. Tech Mess 2018;85:541–52. https://doi.org/10.1515/teme-2017-0086.

[13] Song HC, Kim SW, Kim HS, Lee DG, Kang CY, Nahm S. Piezoelectric Energy Harvesting Design Principles for Materials and Structures: Material Figure-of-Merit and Self-Resonance Tuning. Adv Mater 2020;32:1–34. https://doi.org/10.1002/adma.202002208.

[14] Wei C, Jing X. A comprehensive review on vibration energy harvesting: Modelling and realization. Renew Sustain Energy Rev 2017;74:1–18. https://doi.org/10.1016/j.rser.2017.01.073.

[15] Bowen CR, Topolov VY, Kim HA. Springer Series in Materials Science- Modern Piezoelectric Energy- Harvesting Materials. vol. 238. 2016.

[16] Malakooti MH, Patterson BA, Hwang HS, Sodano HA. ZnO nanowire interfaces for high strength multifunctional composites with embedded energy harvesting. Energy Environ Sci 2016;9:634–

43. https://doi.org/10.1039/c5ee03181h.

[17] Kurita H, Wang Z, Nagaoka H, Narita F. Fabrication and mechanical properties of carbon-fiber-reinforced polymer composites with lead-free piezoelectric nanoparticles. Sensors Mater 2020;32:2453–62. https://doi.org/10.18494/SAM.2020.2820.

[18] Kageyama K, Yoshikawa T, Kato H. Variation in electrical properties of laminates with woven carbon fabric and ferroelectric or piezoelectric particulate epoxy due to tensile loading. Mater Trans 2005;46:697–703. https://doi.org/10.2320/matertrans.46.697.

[19] Wang Z, Kurita H, Nagaoka H, Narita F. Potassium sodium niobate lead-free piezoelectric nanocomposite generators based on carbon-fiber-reinforced polymer electrodes for energy-harvesting structures. Compos Sci Technol 2020;199:108331. https://doi.org/10.1016/j.compscitech.2020.108331.

[20] Alsaadi A, Shi Y, Pan L, Tao J, Jia Y. Vibration energy harvesting of multifunctional carbon fi bre composite laminate structures 2019;178:1–10.

[21] Jia Y, Wei X, Xu L, Wang C, Lian P, Xue S, et al. Multiphysics vibration FE model of piezoelectric macro fibre composite on carbon fibre composite structures. Compos Part B Eng 2019;161:376–85. https://doi.org/10.1016/j.compositesb.2018.12.081.

[22] Saxena KK, Das R, Calius EP. Three Decades of Auxetics Research − Materials with Negative Poisson's Ratio: A Review. Adv Eng Mater 2016;18:1847–70. https://doi.org/10.1002/adem.201600053.

[23] Mir M, Ali MN, Sami J, Ansari U. Review of mechanics and applications of auxetic structures. Adv Mater Sci Eng 2014;2014:1–18. https://doi.org/10.1155/2014/753496.

[24] Li Q, Kuang Y, Zhu M. Auxetic piezoelectric energy harvesters for increased electric power output. AIP Adv 2017;7. https://doi.org/10.1063/1.4974310.

[25] Ferguson WJG, Kuang Y, Evans KE, Smith CW, Zhu M. Auxetic structure for increased power output of strain vibration energy harvester. Sensors Actuators, A Phys 2018;282:90–6.

https://doi.org/10.1016/j.sna.2018.09.019.

[26] Umino Y, Tsukamoto T, Shiomi S, Yamada K, Suzuki T. Development of vibration energy harvester with 2D mechanical metamaterial structure. J Phys Conf Ser 2018;1052. https://doi.org/10.1088/1742-6596/1052/1/012103.

[27] Eghbali P, Younesian D, Farhangdoust S. Enhancement of piezoelectric vibration energy harvesting with auxetic boosters. Int J Energy Res 2020;44:1179–90. https://doi.org/10.1002/er.5010.

[28] Eghbali P, Younesian D, Moayedizadeh A, Ranjbar M. Study in circular auxetic structures for efficiency enhancement in piezoelectric vibration energy harvesting. Sci Rep 2020;10:1–11. https://doi.org/10.1038/s41598-020-73425-1.

[29] ASTM. Standard Test Method for Core Shear Properties of Sandwich Constructions by Beam. Astm C393-06 2006;i:1–9.

[30] Raise3D Premium ABS Technical Data Sheet 2019;270:3–5.

[31] Lakes RS. Cellular solids. J Biomech 1989;22:397. https://doi.org/10.1016/0021-9290(89)90056-0.

[32] Li C, Shen HS, Wang H. Nonlinear Vibration of Sandwich Beams with Functionally Graded Negative Poisson's Ratio Honeycomb Core. Int J Struct Stab Dyn 2019;19. https://doi.org/10.1142/S0219455419500342.

[33] XPREG. XA120 Prepreg Adhesive film technical data sheet 2017;44:2–3.

[34] Lei A, Xu R, Thyssen A, Stoot AC, Christiansen TL, Hansen K, et al. MEMS-based thick film PZT vibrational energy harvester. Proc IEEE Int Conf Micro Electro Mech Syst 2011;1:125–8. https://doi.org/10.1109/MEMSYS.2011.5734377.

[35] Alamin Dow AB, Bittner A, Schmid U, Kherani NP. Design, fabrication and testing of a piezoelectric energy microgenerator. Microsyst Technol 2014;20:1035–40.

https://doi.org/10.1007/s00542-014-2116-9.

[36] XC130 300g Unidirectional Prepreg Carbon Fibre (300mm) n.d. https://www.easycomposites.co.uk/xc130-300g-unidirectional-prepreg-carbon-fibre.

[37] Smart Material. Macro Fiber Composite (MFC) Datasheet 2017:8.

[38] Avvari PV, Yang Y, Soh CK. Long-term fatigue behavior of a cantilever piezoelectric energy harvester. J Intell Mater Syst Struct 2017;28:1188–210. https://doi.org/10.1177/1045389X16667552.

[39] Sushmita, M. Rajesh, Hemanth K., Ravikantha Prabhu, Sharath Meloth C. BKG. Processing and Testing of Hybrid Sandwich Composites for Vibration Damping and Mechanical Properties. J Mech Eng Autom 2016;6:22–7. https://doi.org/10.5923/c.jmea.201601.05.

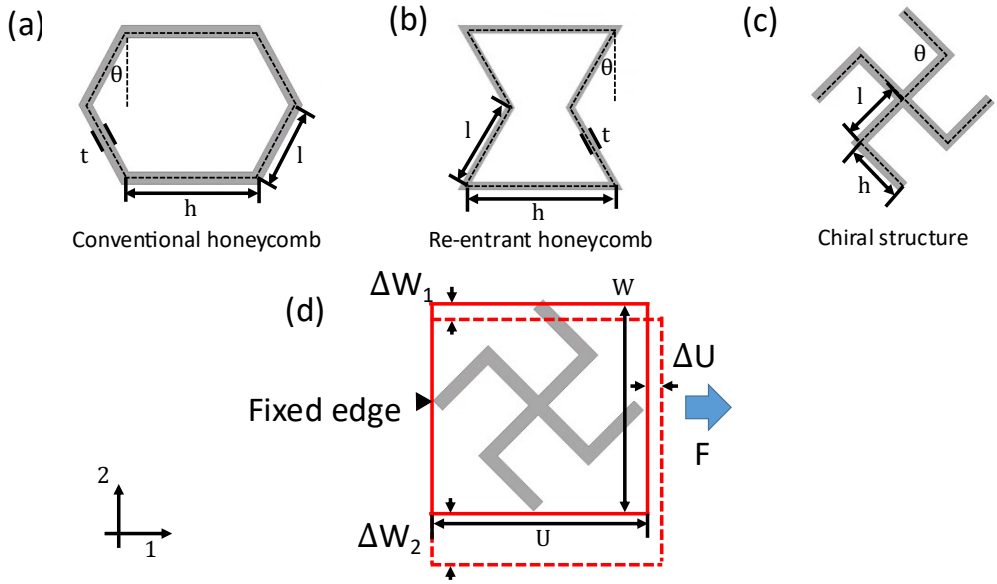

Figure 1 Schematic illustration of unit cell of (a) conventional honeycomb (b) re-entrant honeycomb and (c) chiral structure, (d) FE model to predict the longitudinal Young's modulus and in-plane Poisson's ratio of chiral unit cell

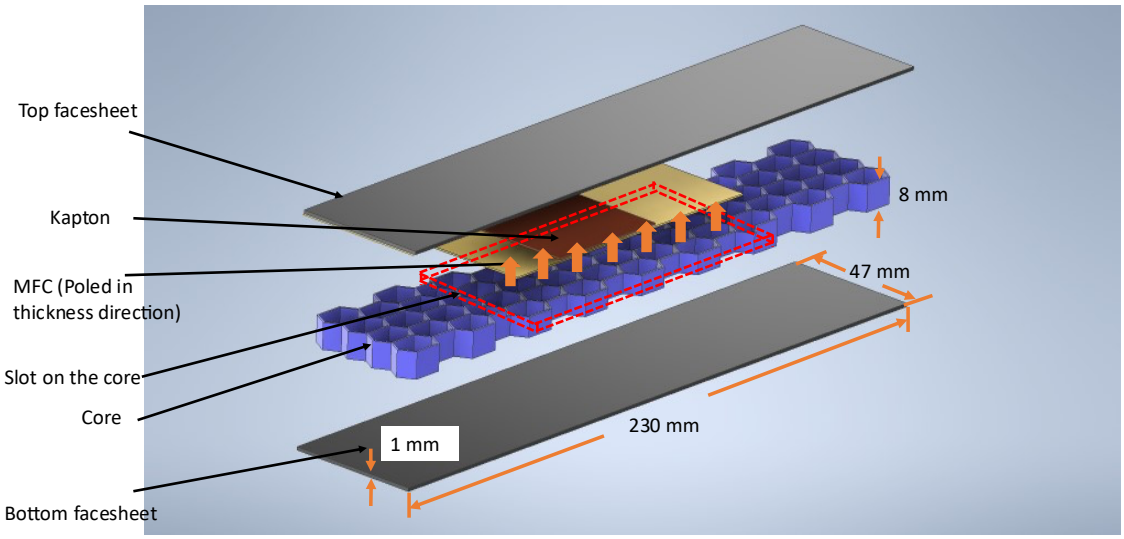

Figure 2 Schematic illustration of sandwich integrated with MFC

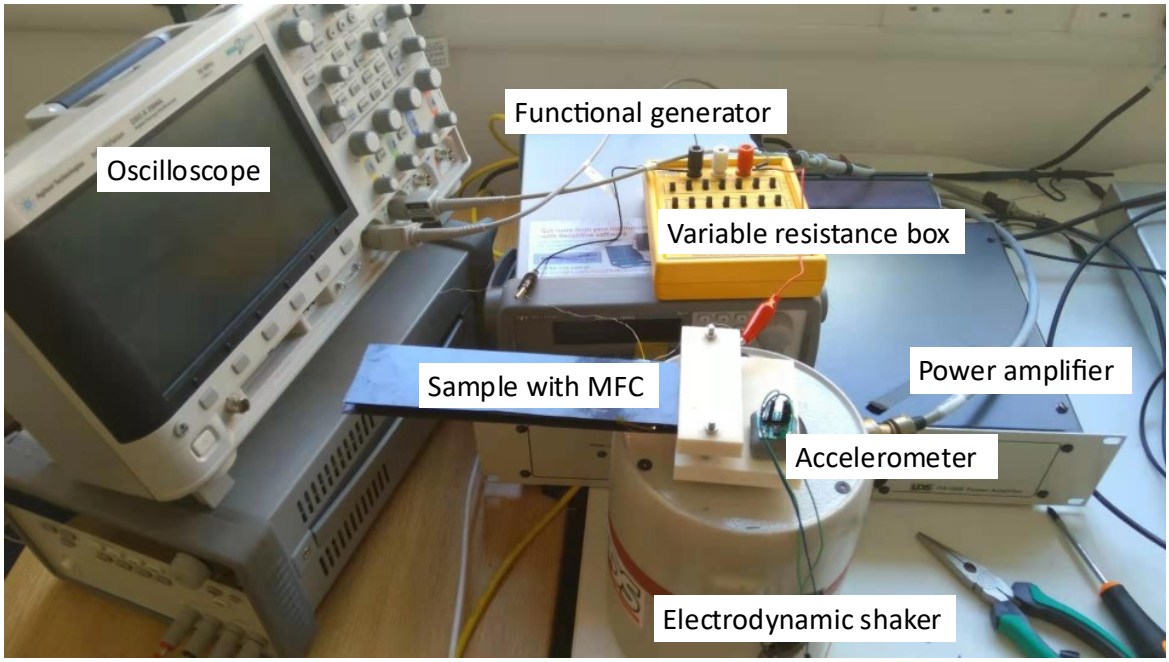

Figure 3 Testing system for energy harvesting experiments

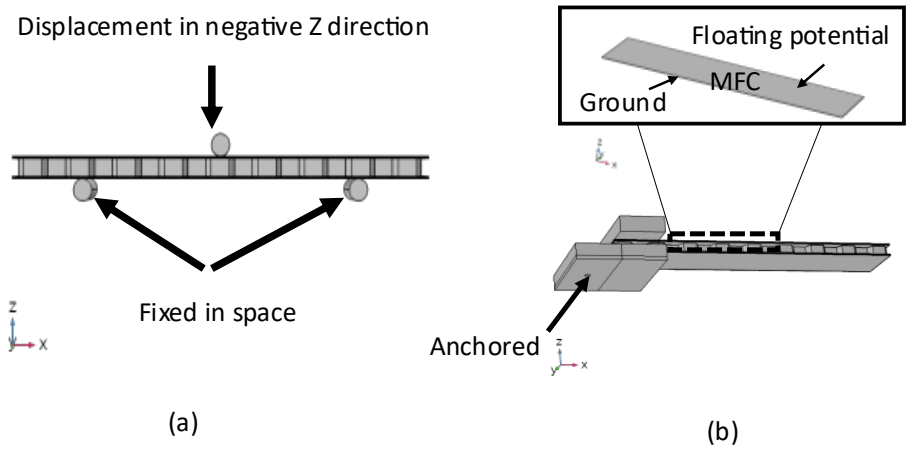

Figure 4 Models and BCs of (a) sandwich under three-point bending (b) sandwich and clamper for energy harvesting (only conventional honeycomb illustrated here as example)

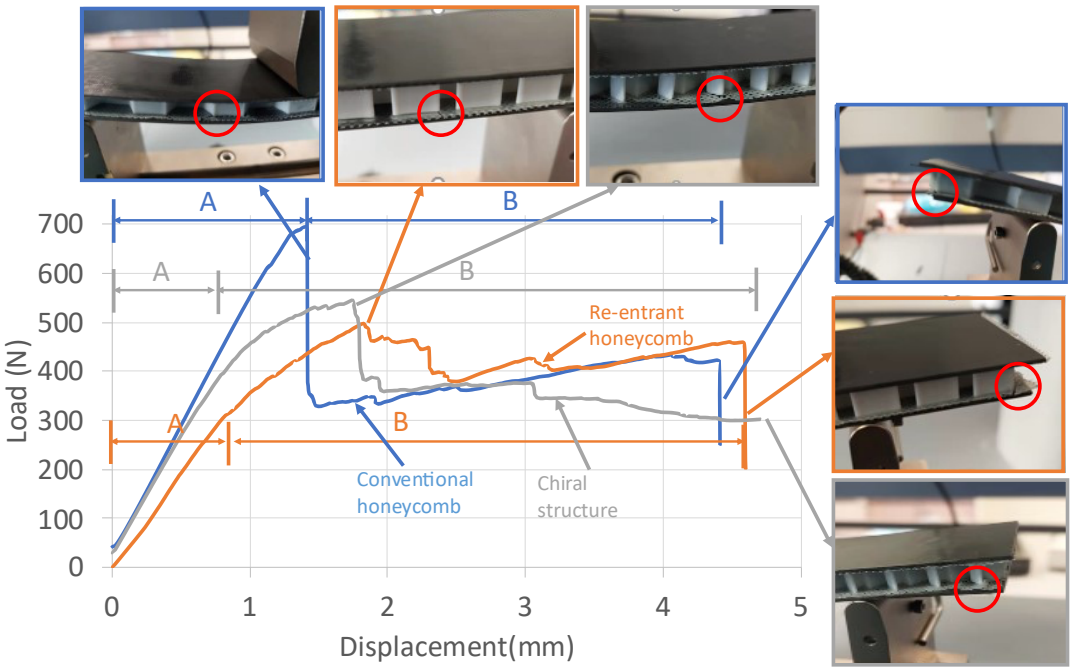

Figure 5 Load-displacement curve of conventional honeycomb core, re-entrant honeycomb core and chiral strurture core sandwich with $[0/90]_s$ facesheet, and the experimental pictures indicating failure mechanisms at different stages

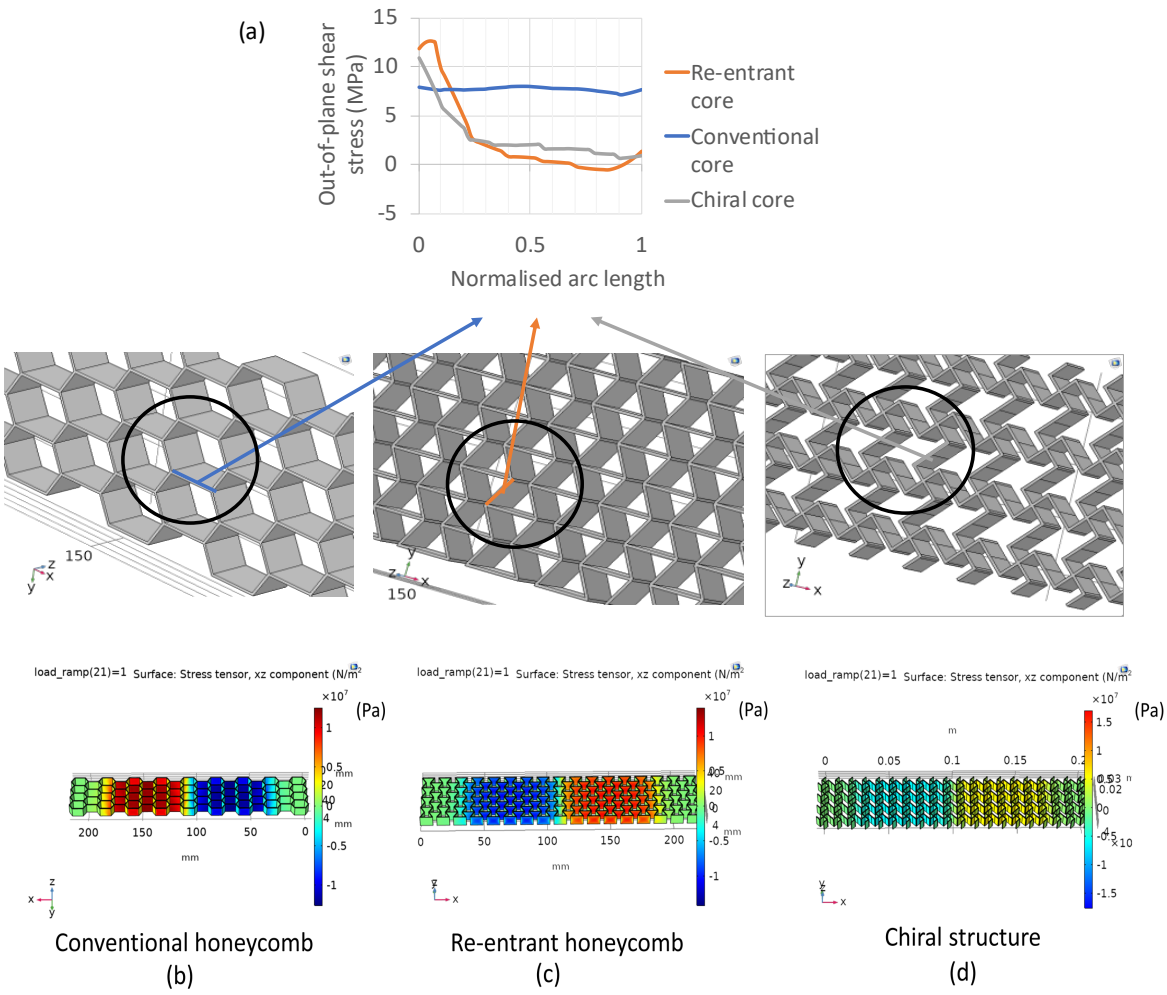

Figure 6 FEA simulation result of (a) out-of-plane shear stress a cell wall ligament at critical location at the interface and shear stress distribution under 3-point bending in the core of (b) conventional honeycomb, (c) re-entrant honeycomb and (d) chiral structure, respectively

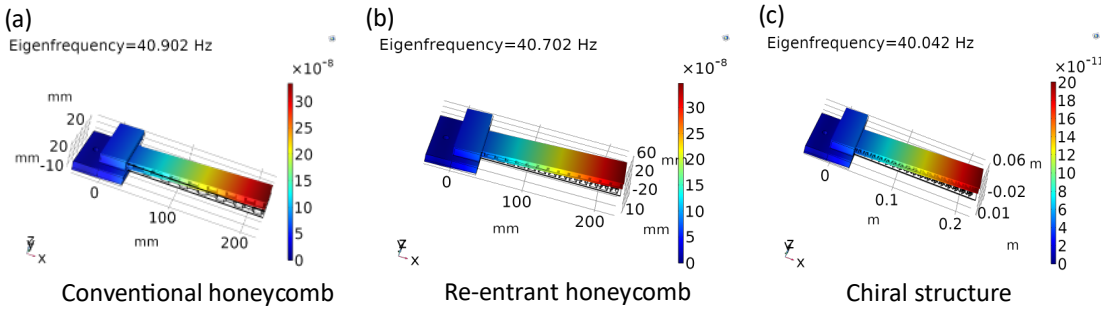

Figure 7 The 1st bending mode shapes and eigenfrequencies for sandwich with (a) conventional honeycomb core (b) re-entrant honeycomb core and (c) chiral structure core (Color bar: Total displacement (m))

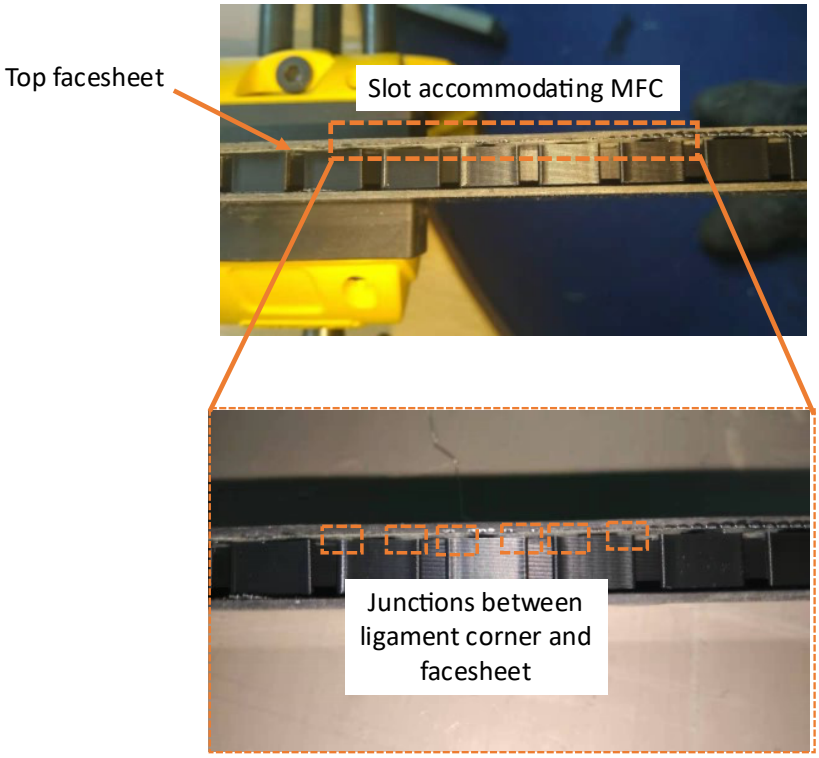

Figure 8 Side view of sandwich with re-entrant honeycomb core with core-facesheet junction at location of the slot

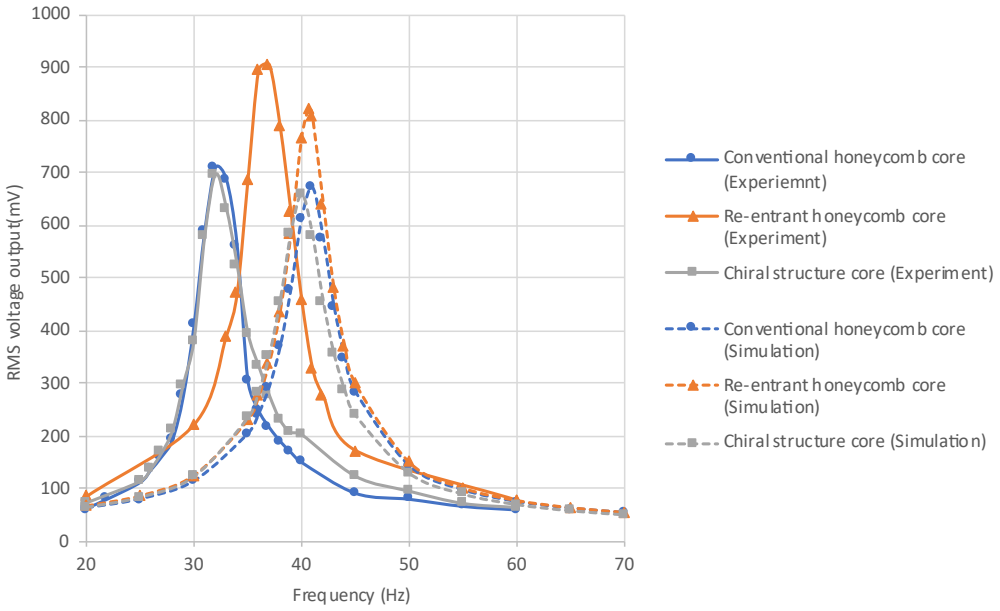

Figure 9 RMS voltage output under open-circuit condition for experimental measurement, under 1 g peak-peak input acceleration and 10 MΩ external resistance

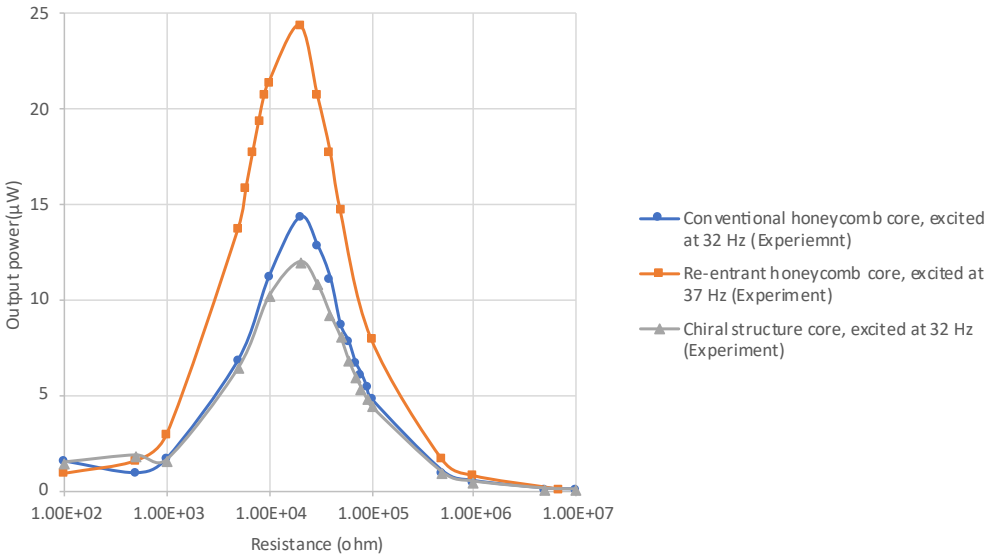

Figure 10 Comparison of output power under different external loading between different core topology design, under 1 g peak-peak input acceleration, excited at 1st bending mode resonant frequencies

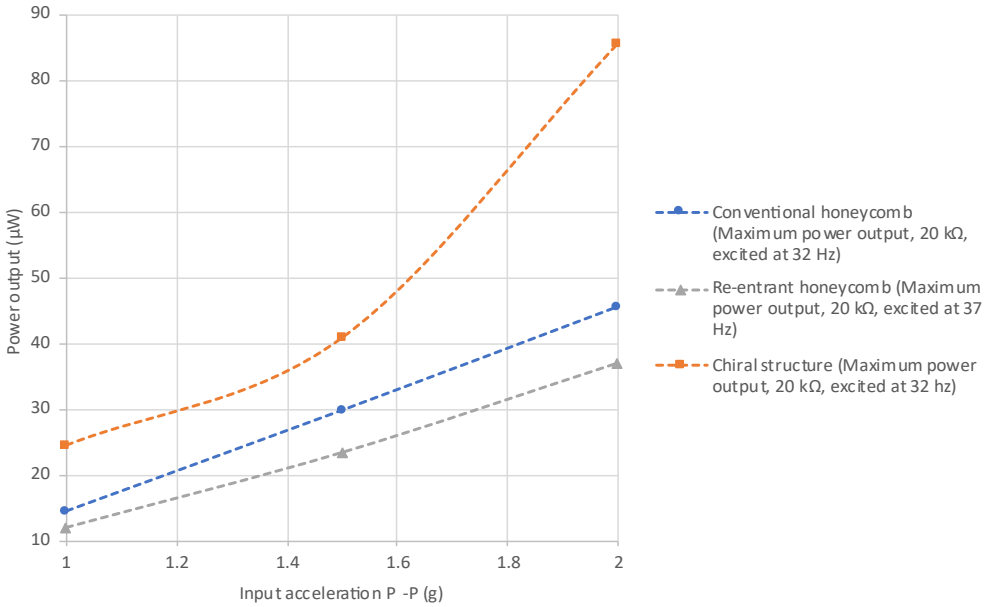

Figure 11 Maximum power evolution with increase of input acceleration at 1st bending mode resonant frequencies and 20 kΩ optimum external resistance

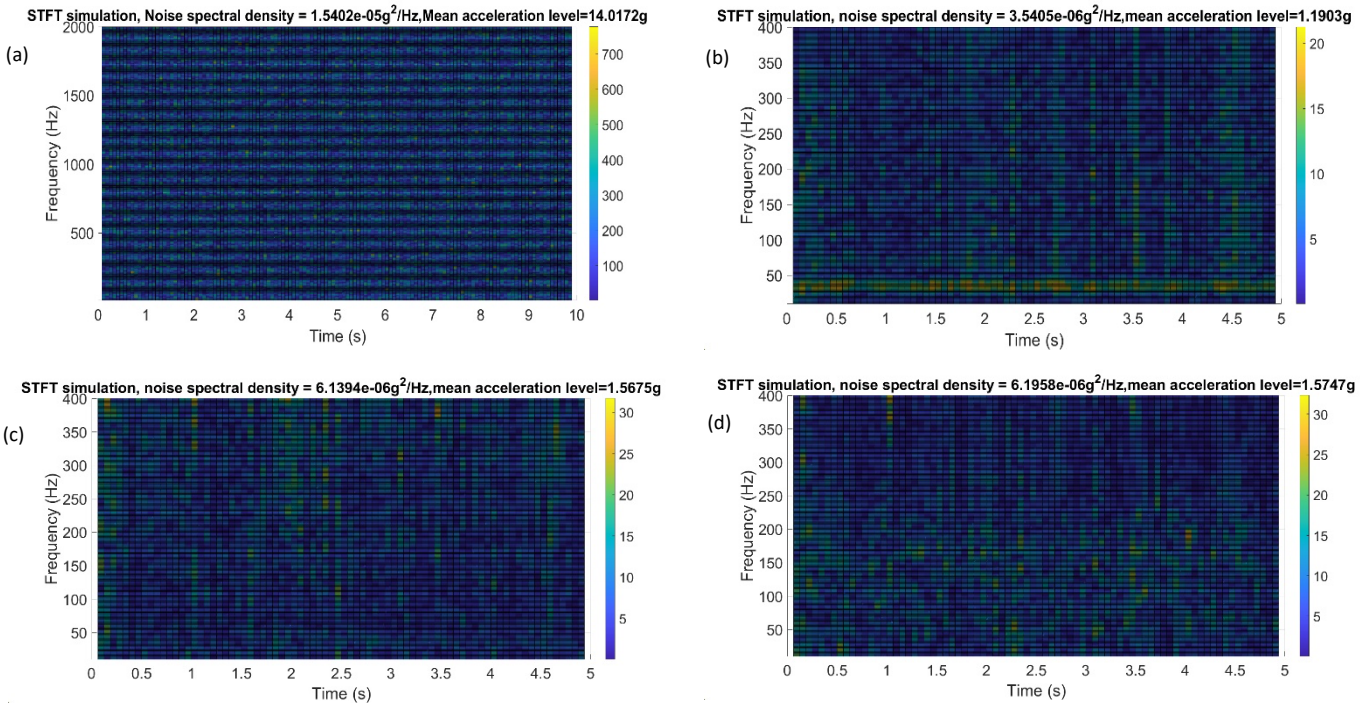

Figure 12 Short-time Fourier Transform (unit: g) of acceleration data of (a) an in-flight CGJ aircraft, (b) x-axis (along the car), (c) y-axis (across the car) and (d) z-axis (upright direction) of a BWM vehicle [19, 20]

Table 1 Dimensions of cellular unit cells and contour dimension of cellular topologies

	h(mm)	l(mm)	θ(˚)	t(mm)	Overall sandwich dimension (mm*mm*mm)
Conventional	10	6	30	0.9	225*42*8
Re-entrant	10	6	-30	0.5	221*42*8
Chiral	4	4	90	0.75	227*46*8

Table 2 Material properties of CFRP, ABS cellular structures and MFC P2-8528 used in the simulation [30, 37]

Topological properties			
	Conventional honeycomb	Re-entrant honeycomb	Chiral structure
Young's modulus E_1^{eff} (MPa)	24.7	2.2	3.9
Poisson's ratio v_{12}^{eff}	0.69	-1.29	-0.07
Relative density ρ_{rel}	0.148	0.151	0.150
Mechanical property of CFRP			
Young's modulus (GPa)	E_x	E_y	E_z
	135	6.2	6.2
Shear modulus (GPa)	G_{xy}	G_{xz}	G_{yz}
	4.83	4.83	2.66
Poisson's ratio (1)	v_{xy}	v_{xz}	v_{yz}
	0.25	0.25	0.42
Density (kg/m^3)	1628		
Mechanical property of ABS			
Young's modulus (GPa)	2.2		
Poisson's ratio (1)	0.35		
Density (kg/m^3)	1120		
Mechanical (constant electrical field), piezoelectric and dielectric (constant stress) properties of MFC			
Compliance matrix (Voigt notation) (1/GPa)	S_{11}^E	S_{12}^E	S_{13}^E
	0.033	-0.010	-0.010
	S_{22}^E	S_{23}^E	S_{33}^E
	0.063	-0.019	0.063
	S_{44}^E	S_{55}^E	S_{66}^E
	0.164	0.181	0.181
Density (kg/m^3)	5400		
Piezoelectric constant d_{33}^T (pC/N)	400		
Piezoelectric constant d_{31}^T (pC/N)	-170		
Capacitance per unit area (nF/cm^2)	7.8		
Relative permittivity ε_{33}^T	1695		

Table 3 Comparison of energy absorption performance between sandwiches of different core topologies

	Conventional honeycomb	Re-entrant honeycomb	Chiral structure
Rigidity(N/mm)(std%)	559.44 (2.09%)	416.09(0.82%)	473.42 (3.08%)
Maximum loading(N)(std%)	787.66 (11.50%)	470.19(6.24%)	521.58 (4.66%)
Crashing force efficiency (std%)	0.59 (6.76%)	0.78(2.20%)	0.69 (5.66%)
Energy absorption (J) (std%)	1.88(9.57%)	1.66(4.22%)	1.69 (0.30%)
Specific energy absorption (J/g) (std%)	0.035(9.46%)	0.028(0.10%)	0.027(0.40%)

Table 4 Comparison of 1st bending mode resonant frequency and RMS open-circuit voltage output at 1st bending resonance between experimental measurement and simulation result

	1st bending mode resonance (Hz)		**1st mode damping ratio**	**RMS open-circuit voltage output at resonance (mV)**	
	Experiment	FE simulation	Experiment	Experiment	FE simulation
Conventional honeycomb	32	41(+21.9%)	0.046	710	672(-5.4%)
Re-entrant honeycomb	37	40(+7.5%)	0.041	906	824(-9.1%)
Chiral structure	32	40(+20.0%)	0.048	696	657(-5.6%)

Table 5 Simulation result of volume average stress towards longitudinal and transverse direction and their summation

	σ_{11} volume average (kPa)	**σ_{22} volume average (kPa)**	**$(\sigma_{11}+\sigma_{22})^2$ (kPa^2)**
Conventional honeycomb	41.88	-11.08	948.64
Re-entrant honeycomb	43.52	-12.24	978.44
Chiral structure	42.91	-11.81	967.21

Table 6 Results of existing works on piezoelectric energy boost utilizing auxetic design in substrate

Ref.	Structure	Transducer	Characterization	Output(enhancement compared to non-auxetic counterpart)
[25]	Steel beam with Re-entrant honeycomb	PZT	250 με tensile strain at 10 Hz	142.2 μW (1061%)
[27]	Steel beam with ancient-motif auxetic shape	PZT	2.5e6 N/m^3 periodic body load at 20 Hz	2.03 mW(548%)
[26]	Re-entrant honeycomb core	PVDF (as facesheet covering the core)	Base excitation at resonance	47.4 μW(159%)
[24]	Metallic sheet with orthogonally arranged elliptical voids	PVDF	0.1 mm tension at 10 Hz	650 μW (282%)
[28]	PLA beam with circular auxetic structure	PZT 4D	Base excitation at resonance	60 μW (around 1200%)
Present work	Sandwich with re-entrant honeycomb core	MFC P2-8528	Base excitation at resonance	24.4 μW (around 200%)

Table 7 Comparison of power output between sandwiches with different core topologies when excited by real-world vibration

	Aerospace (μW)(14.02 g mean acceleration)	Road car x axis(μW) (1.19 g mean acceleration)	Road car y axis(μW) (1.57 g mean acceleration)	Road car z axis(μW) (1.57 g mean acceleration)
Conventional honeycomb	22191.1	156.71	710.01	143.47
Re-entrant honeycomb	33262.1	344.39	692.22	204.91
Chiral structure	17717.7	128.97	298.04	100.51